Cellulose
https://doi.org/10.1007/s10570-024-06117-y

ORIGINAL RESEARCH

Injectable and printable nanocellulose-crosslinked quaternary chitosan blends for potential wound healing

Maryam Madani · Isabella Laurén · Sedigheh Borandeh · Zahra Gounani · Timo Laaksonen · Nina Lindfors · Jukka Seppälä

Received: 23 April 2024 / Accepted: 10 August 2024

Abstract Developing hydrogels with excellent 3D printability, injectability, and mechanical integrity presents an imposing challenge in biomaterials research, especially in the biomedical field where biocompatibility is crucial. This study involved the development of 3D printable and injectable polysaccharide-based hydrogels with inherent self-healing capabilities. Carboxymethyl chitosan and quaternized chitosan (QCS) functioned as polymer backbones, reinforced by dialdehyde-cellulose nanocrystals (DACNC) as a cross-linker. Here, the concentrations of QCS and DACNC were adjusted and optimized for ideal performance. The cross-linking process was orchestrated in situ, integrating dynamic hydrogen bonds and Schiff base covalent bonds to achieve a multi-cross-linked hydrogel network. Comprehensive characterization of the material, including rheological measurements and macroscopic evaluations, demonstrated the hydrogel's admirable injectability, printability, and self-healing attributes. In vitro cell viability assessments on human dermal fibroblasts revealed favorable biocompatibility and minimal cytotoxicity of the hydrogels, properties influenced by the concentrations of QCS. The obtained hydrogels exhibit promising attributes suitable for fabricating 3D printable and injectable hydrogel customized for biomedical applications, particularly wound healing.

Maryam Madani and Isabella Laurén have contributed to this work.

Supplementary Information The online version contains supplementary material available at https://doi.org/10.1007/s10570-024-06117-y.

M. Madani · I. Laurén · S. Borandeh · J. Seppälä (✉)
Polymer Technology, School of Chemical Engineering, Aalto University, 02150 Espoo, Finland
e-mail: jukka.seppala@aalto.fi

Z. Gounani · T. Laaksonen
Division of Pharmaceutical Biosciences, Faculty of Pharmacy, University of Helsinki, 00790 Helsinki, Finland

N. Lindfors
Department of Hand Surgery, Helsinki University Hospital, University of Helsinki, 00290 Helsinki, Finland

Published online: 14 August 2024

Graphical abstract

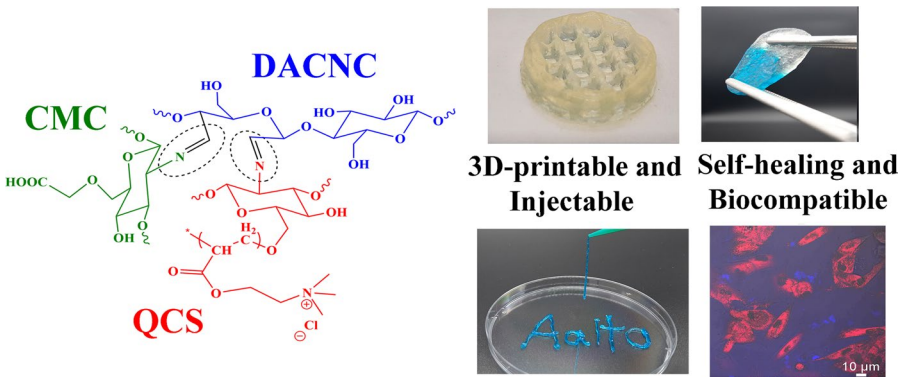

Keywords Quaternized chitosan · Cellulose nanocrystals · Injectable hydrogel · Wound-healing

Introduction

3D printing has become a standard technique for designing wound dressings, wherein hydrogel bioinks emerge as excellent candidates for this purpose, compatible with extrusion, laser, or inkjet printing methods (Wang et al. 2019; Zhou et al. 2019). However, a common issue observed in naturally derived hydrogels used for 3D printing is their susceptibility to collapse and low shape integrity due to their soft composition. Utilizing amines and aldehyde groups in Schiff's reactions has been explored as a method for fabricating injectable hydrogels, offering a rapid process that occurs under ambient conditions among various techniques for hydrogel formation. These injectable hydrogels exhibit notable stability and biocompatibility, making them valuable for various tissue engineering applications (Kim et al. 2019; Xu et al. 2019). Conversely, traditional wound dressings often incorporate antimicrobial agents within the hydrogel matrix, such as silver, zinc oxide, or antibiotics. Yet, using dressings with inherent antimicrobial properties holds greater appeal. Chitosan is renowned for its role in the preparation of antimicrobial dressings due to the easy formation of quaternary ammonium cations under acidic conditions (Hamedi et al. 2018; Qing et al. 2021). Nevertheless, chitosan requires modifications to overcome its limited solubility and inadequate biological properties under neutral and alkaline conditions. In our previous studies, we demonstrated enhanced antimicrobial activity by introducing quaternary compounds to chitosan, with emphasis on the appealing antimicrobial performance of quaternized chitosan (QCS) featuring [2-(acryloyloxy)ethyl]-trimethylammonium chloride (AETMAC) (Borandeh et al. 2023).

Despite the inherent biocompatibility and biodegradability of natural hydrogels, they have drawbacks, including substandard mechanical and physical attributes. In recent decades, efforts have been focused on enhancing the mechanical properties of hydrogels, resulting in the development of novel hydrogel structures such as dual-crosslinked, double-network, and nanocomposite hydrogels (Fan et al. 2013; Lin et al. 2015; Wang et al. 2018). Previous studies have explored hydrogel structures comprising various polysaccharides, including dialdehyde cellulose nanocrystals (DACNC) and functionalized chitosan derivatives. DACNCs possess dual functionality as reinforcement and cross-linkers due to their large surface area, high aspect ratio, and sturdy mechanical properties. Previous studies include the development of various polysaccharide-based hydrogels, often incorporating DACNC and various modified cellulose and chitosan derivatives, focusing on aspects such as biocompatibility, injectability, and optimization of mechanical properties (Huang et al. 2018; Wei et al. 2022).

Building upon our previous discoveries, this study aimed to develop a series of multi-crosslinked double-network hydrogels suitable as wound-healing barriers. These hydrogels are envisioned to encompass a unique combination of attributes, including self-healing capability, 3D printing proficiency, injectability, and intrinsic biocompatibility. Dynamic covalent bonds like Schiff base bonds can achieve such self-healing properties of hydrogels (Quan et al. 2022). The hydrogel design is based on integrating carboxymethyl chitosan (CMC), QCS, and DACNCs, using reversible Schiff's base reactions, with a key focus on the liquid-to-solid transition. CMC functions as the matrix polymer to improve the viscosity and printability of the gels, whereas QCS provides biocompatibility and potential antimicrobial properties to the hydrogels. The properties of QCS are based on the results of our previous studies, where AETMAC-modified chitosan showed superior antimicrobic capabilities and solubility to GTMAC-modified derivatives (Borandeh et al. 2023; Teotia et al. 2023). DACNC functions as the cross-linker between the polysaccharides and as reinforcement for the hydrogel structure. This investigation delves into the impact of compound concentration ratios on physiochemical and biological properties. A comprehensive evaluation of the hydrogel's rheological properties, printability, self-healing, and biocompatibility was undertaken. These materials are promising biocompatible barrier layers in wound-healing applications or other tissue engineering endeavors.

Experimental Section

Materials

Powdered cellulose nanocrystals (CNC) (D = 5 nm, L = 100 nm, aspect ratio = 20) were provided by Celluforce Inc. (Canada). [2-(acryloyloxy)ethyl]-trimethylammonium chloride solution (AETMAC) and ammonium persulfate (98%) (APS) were obtained from Sigma Aldrich (USA). Sodium metaperiodate ($NaIO_4$) was purchased from Alfa Aesar (USA), whereas sodium hydroxide (NaOH), benzaldehyde (C_7H_6O), and sodium hydrogen carbonate ($NaHCO_3$) were obtained from Merck (Germany). Carboxymethyl chitosan (CMC) (CAS No. 83512-85-0, DDA ≥ 80) was purchased from Biosynth Carbosynth (UK), and chitosan (CAS No. 9012-76-4, DDA ≥ 75%, M_w = 60 kDa) from TCI (Japan). All compounds were used as received without any further purifications. Dulbecco's Modified Eagle Medium (DMEM) GlutaMAXTM (Cat. No. 31966047) and fetal bovine serum were obtained from Gibco/Thermo Fischer (USA). Alamar Blue™ Cell Viability Reagent was purchased from Invitrogen (Finland).

Preparation of dialdehyde CNCs (DACNCs) by oxidation

We followed a procedure inspired by previous reports for the oxidation of CNC, with minor modifications (Dang et al. 2019; Lu et al. 2014). Briefly, a 3 wt% suspension of CNC was prepared in deionized water, and $NaIO_4$ (1:1 w/w $NaIO_4$/CNC) was added. The pH of the suspension was carefully adjusted to 3.0 and stirred for 3 h at 40 °C. The beaker was covered with aluminum foil to shield the reaction from light interference. To terminate the reaction and remove residual sodium periodate, ethylene glycol was added, and the mixture was stirred for 1 h. The resultant suspension underwent centrifugation to separate the oxidized CNC from the reaction by-products, and the isolated material was washed three times with deionized water. To ensure maximum purity, the isolated oxidated CNCs underwent a three-day dialysis process against deionized water using a cellulose membrane (M_w cut-off 14 kDa). The degree of aldehyde modification was 32% as determined by titration. The crystallinity of CNC and DACNC was estimated according to the Segal empirical method based on the XRD pattern in Fig. S2, determined as 68.73% for the DACNC and 81.97% for CNC (Segal et al. 1959).

Preparation of quaternized chitosan (QCS)

The QCS was prepared according to our previous publications (Borandeh et al. 2023; Teotia et al. 2023). Chitosan was quaternized in the *O*-position to ensure further reaction through the more reactive amine. Before quaternization, the amine was protected by benzaldehyde (generating Schiff's base chitosan) to ensure quaternization solely in the O-6 position. After quaternization, the amine was deprotected. The details of the whole radical polymerization

Table 1 Amounts of dry CMC, DQC, and DACNC in the formations of the hydrogel inks

Sample	CMC [mg]	QCS [mg]	DACNC [mg]
HA1	1 000	200	60
HA2	1 000	200	120
HA3	1 000	200	180
HB1	1 000	400	60
HB2	1 000	400	120
HB3	1 000	400	180
HC1	1 000	600	60
HC2	1 000	600	120
HC3	1 000	600	180

reaction are found in SI and Fig. S1. The degree of quaternization (dQ) of the obtained QCS was determined by assessing ^{1}H NMR integrals, denoted as dQ = 1.4 in Eq. 1.

$$dQ = \frac{-N^{+}\left(CH_3\right)_3 \times 6}{(H2, H3-H6, H6') \times 9} \quad (1)$$

Here, $N^{+}(CH_3)_3$ and (H2, H3-H6, H6') represent the integrals related to the quaternary ammonium and pyranose protons, respectively. These integrals are illustrated in Fig. S3. The molecular weight was estimated as 5.1 kDa, per previous estimations (Teotia et al. 2023).

Preparation of DACNC-CMC-QCS inks

DACNC-CMC-QCS hydrogel inks were prepared through the introduction of various concentrations of QCS (200, 400, and 600 mg) and DACNC (60, 120, and 180 mg) into an aqueous CMC solution (1000 mg), as seen in Table 1. To outline the procedure briefly, CMC powder was initially dispersed in water to prepare a 10 wt% gel. Subsequently, QCS was introduced into the matrix (at concentrations of 200, 400, and 600 mg), creating uniform solutions. The resulting solutions were designated as HA, HB, and HC, corresponding to the three concentrations of QCS. Following this, varying amounts of DACNCs (60, 120, and 180 mg) were incorporated into each QCS-infused solution, where each resulting hydrogel ink was further denoted as 1, 2, and 3 within their respective hydrogel categories. For instance, within the HA group, three unique hydrogels were prepared, designated as HA1, HA2, and HA3. A total amount of 9 gels was prepared (Table 1). The gelation process was carefully monitored, and the time required for gel formation was recorded for all samples. Visual confirmation of gel formation was obtained by gently inverting the tubes containing the DACNC-CMC-QCS gels.

3D printing and injectability

The hydrogels were printed following ink preparation using an extrusion-based printing technique employing a BIOX bioprinter (CELLINK, Sweden). The inks were poured into 3 mL pneumatic syringes immediately after adding DACNC to the CMC-QCS solution. The inks were extruded at 22 °C through a 20G conical needle (0.63 mm inner diameter) at 5 mm/s. The hydrogels were printed as circles and squares in 5 layers (10 mm diameter). The printing parameters were carefully adjusted through multiple cycles of material optimization, considering the rheological behavior of the inks. This process aimed to ensure the printed structure's repeatability, dimensional accuracy, and stability. The injectability of the inks was tested immediately after preparation with an 18G conical needle (0.84 mm inner diameter).

Characterization

The presence of aldehyde groups of DACNC was determined using Schiff's base reaction between the aldehyde groups and hydroxylamine hydrochloride (Lu et al. 2014). To quantify the dialdehyde content (DC) of DACNC, the following equation was applied:

$$DC(\%) = \frac{C\left(V_1 - V_2\right) \times 162}{M \times 1000} \times 100 \quad (2)$$

where V_1 represents the volume of NaOH utilized by DACNC (mL); V_2 signifies the volume of NaOH consumed by CNC (mL); C is the concentration of NaOH (mol/L), and M is the weight of each sample (g). The chemical structure of the materials was investigated at room temperature with an attenuated total reflectance (ATR–IR) Perkin Elmer spectrometer in transmission mode. The samples were scanned within the range of 4000–500 cm^{-1}, with a resolution of 4 cm^{-1} with 32 accumulations. The rheological characteristics were conducted using

an Anton Paar Physica MCR 301 (Austria) rheometer with parallel plates (PP25 and CP25 geometries). A fixed gap of 49 µm and CP25 geometry were utilized to monitor the apparent shear viscosity of the gels. A strain sweep ranging from 0.01 to 100% at a consistent frequency of 1 rad s^{-1} with a fixed gap of 1 mm was further conducted to precisely determine the linear viscoelastic range of the hydrogels based on the PP25 geometry. To evaluate the hydrogel's capacity for recovery following strain deformation, they were repeatedly subjected to oscillating strains of 1 and 200% at intervals of 200 s, all while maintaining a frequency of 1 Hz. The compression stress–strain curves were obtained using an Instron Universal testing machine (model 5944) with a 50 N load cell. Hydrogels HA2, HB2, and HC2 were first equilibrated in water and then subjected to compression at a constant rate of 0.1 mm/min under controlled conditions (25 °C and 50% relative humidity).

Scanning Electron Microscope (SEM) images of the hydrogels were acquired with a Scanning Electron Microscope (Zeiss Sigma VP microscope, Germany) at a voltage of 5 kV. The images were captured following the sputter coating of freeze-dried hydrogels with a thin 4 nm layer of gold–palladium alloy (LEICA EM ACE600 sputter coater, Germany).

Self-healing behavior

The self-healing properties of the hydrogels were assessed through macroscopic evaluation. Briefly, a hydrogel (20 mm in diameter and 1 mm thick) was initially cut into two separate pieces. These divided hydrogel segments were reassembled and allowed to self-heal for 1 h under ambient conditions. Following the self-healing period, manual stretching was applied to the hydrogel, and photographic documentation was conducted to capture the results. Furthermore, to gain a deeper understanding of the self-healing characteristics, a rheological study was conducted on the hydrogel (Fan et al. 2021).

Swelling capacity

The swelling behavior of the obtained hydrogels was determined by measuring the water absorption of the dried samples for 24 h, following the previously described methods (Baniasadi et al. 2021; Janarthanan et al. 2020). The hydrogels were freeze-dried, weighted (m_0), and immersed in phosphate buffer (pH 7.4). The samples were taken out after 1.5, 3, 6, and 24 h, gently dried using tissue paper, and weighed immediately (m_i). The swelling ratio of the hydrogels was calculated using Eq. 3.

$$\text{Swelling } (\%) = \frac{m_i - m_0}{m_0} \times 100 \tag{3}$$

Hydrolytic degradation

The hydrolytic degradation of the hydrogels was evaluated by monitoring their weight loss over 9 days, according to previously described procedures (Baniasadi et al. 2021; Janarthanan et al. 2020). The samples were freeze-dried, weighted (m_0), and immersed in phosphate buffer (pH 7.4) at 37 °C. The hydrogels were taken out, thoroughly vacuum-dried for 24 h, and weighted (m_j) after 1, 4, 6, and 9 days of submersion. The weight loss of the hydrogel was determined using Eq. 4. The gel content, representing the degree of crosslinking within the hydrogel network, was determined based on dry-weight differences. Dry hydrogels were immersed in water for 24 h and subsequently vacuum-dried at 40 °C for an additional 24 h.

$$\text{Weightloss } (\%) = \frac{m_0 - m_j}{m_0} \times 100 \tag{4}$$

Cell viability assay

The biocompatibility of the obtained hydrogel scaffolds was evaluated on human dermal fibroblast (HDF) cells (HDFn, PCS-201-010) cultured in DMEM GlutaMAXTM (Gibco/Thermo Fischer) medium supplemented with 10% FBS at 37 °C in a 5% CO_2. The hydrogels (100 mg in microtubes) were sterilized using wet autoclaving before culturing. The cell viability was assessed by Alamar Blue™ (Invitrogen). Briefly, the hydrogels were placed in a 24-well plate, and HDF cells were cultured in the wells at 104 cells/well density. Wells containing only media and hydrogels without any cells were used as negative controls, and wells with cells in cell media were used as positive controls. After 1, 3, or 7 days

of incubation, Alamar Blue was added to the media and incubated overnight. The fluorescent intensity of the Alamar Blue was read in an excitation/emission wavelength of 530/560 nm using spectrophotometry (Varioskan Lux, Thermo Fisher Scientific, USA). The cell viability was calculated as the differences in fluorescent intensities, according to Eq. 5:

$$\frac{\text{Intensity of wells with cells on hydrogel} - \text{Intensity of wells with hydrogel only}}{\text{Intensity of wells with cells in media} - \text{Intensity of media}} \quad (5)$$

Cell imaging

For cell imaging, HDF cells were seeded in 8-well plates (Nunc® Lab-Tek® II Chambered Coverglass, Thermo Fischer) at a density of 10^4 cells/well and incubated at 37 °C and 5% CO_2 for 24 h. LysoTracker™ Deep Red (Thermo Fischer, USA) was added to the wells 30 min before imaging at a concentration of 100 nM. The samples were imaged using a confocal laser scanning microscopy (Leica TCS SP8 STED—Stimulated Emission Depletion, Germany). The system was equipped with a diode laser (405 nm excitation wavelength) and HeNe laser (633 nm excitation wavelength) to observe the hydrogels and the LysoTracker™ Deep Red, respectively. Images were obtained using a 63x/1.20 (water, wd = 0.3 mm) objective and analyzed using a LAS X software version 3.7.4.23463 for Leica SP8.

Results and discussion

Hydrogel formation

A double-network hydrogel has been developed, characterized by multiple cross-links, rapid self-healing, and 3D printability. The comprehensive process for creating this hydrogel, based on QCS, CMC, and DACNC, is succinctly illustrated in Fig. 1. Several notable features render these DACNC-CMC-QCS hydrogels well-suited for biomedical applications,

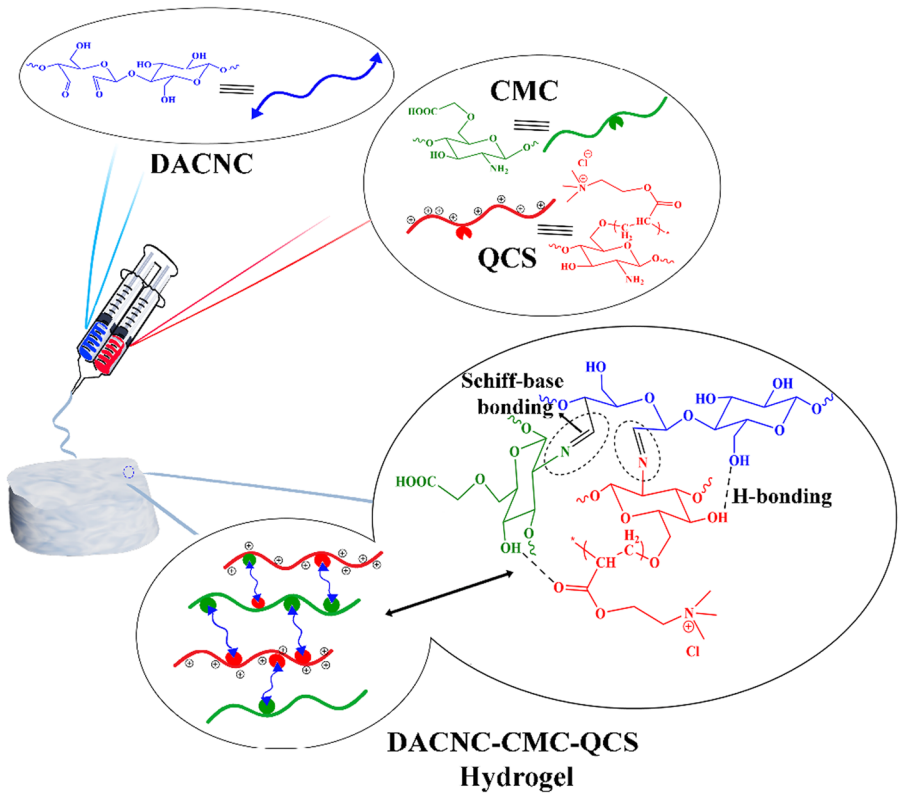

Fig. 1 Schematic image of preparation of injectable and printable DACNC-CMC-QCS hydrogels, illustrating the network formation between positively charged QCS (red), DACNC (blue), and CMC (green)

Table 2 Gel formation time and gel content of DACNC-CMC-QCS hydrogels

Sample	Time [sec]	Gel content [%]
HA1	150	65
HA2	120	83
HA3	90	81
HB1	60	60
HB2	40	83
HB3	30	87
HC1	> 30	62
HC2	> 30	75
HC3	> 30	84

including using water as a solvent, rapid gelation time, and the absence of reliance on external stimuli such as pH, temperature, or light. In addition, due to their self-healing properties, these materials can recover their shape and structure after having been damaged (Li et al. 2020).

The hydrogel formation within the DACNC-CMC-QCS matrix can be attributed to the establishment of double reversible and dynamic Schiff-base linkages (−C=N−), a rapid reaction that takes place under ambient conditions. These bonds form between the amine groups ($-NH_2$) present in the flexible CMC and QCS polymer chains and the aldehyde groups (−CHO) stemming from the rigid rod-like DACNC (Fig. 1). The formation of the linkages was confirmed with both rheological characterization and FT-IR. The stiff, rod-like nature of DACNCs serves the dual purpose of cross-linking within the hydrogels and reinforcing their structure on the nanoscale. The extensive surface area and high aspect ratio of DACNC contribute to the presence of numerous active cross-linking sites, facilitating quick gelation. The gelation time (Table 2) decreased with increased concentrations of both QCS and DACNC. This reduction can be attributed to the accelerated Schiff's base reactions between the primary amines and aldehyde groups. This gel formation process aligns with previously reported mechanisms for forming imine bonds (Huang et al. 2018, 2016). The gel content was significantly lower in the H1-series, as these contained the lowest concentration of DACNC. This suggests that a critical threshold of DACNC concentration is necessary to facilitate the formation of a cross-linked network.

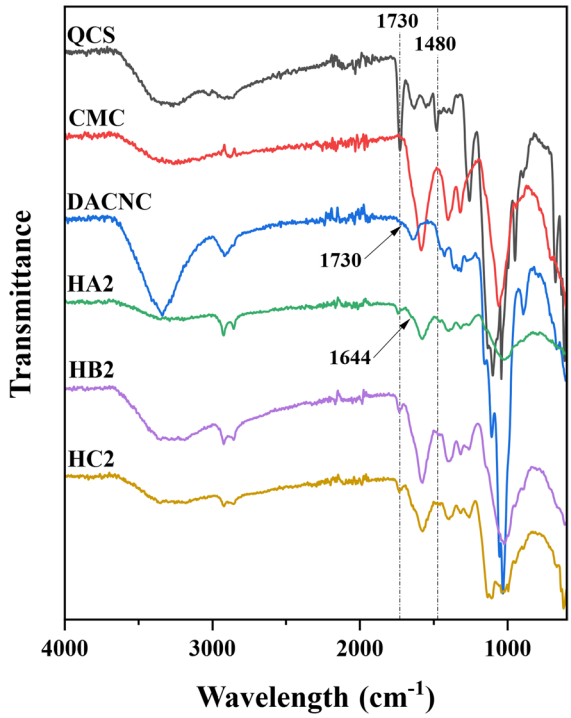

Fig. 2 FT-IR spectra of QCS, CMC, DACNC, and hydrogels containing varying amounts of QCS

FT-IR analysis

The chemical structures of the key components QCS, CMC, and DACNC, as well as the hydrogels HA2, HB2, and HC2, were confirmed through FT-IR analysis (Fig. 2). As shown in Table 1, we prepared nine sets of hydrogels, each containing distinct proportions of QCS and DACNC. To demonstrate the formation of imide bonds and the presence of quaternary ammonium functional groups, we focused on the FT-IR spectra of the dried hydrogels HA2, HB2, and HC2, containing constant concentrations of CMC and DACNC. These specific models were selected due to their variations in QCS concentration, allowing for a comprehensive examination of these chemical attributes. The characteristic peaks related to the QCS are the absorption band at approximately 1730 cm^{-1}, corresponding to the stretching vibrations of the ester groups (C=O), and the asymmetrical stretching of the quaternary ammonium ($-N^+(CH_3)_3$)

seen approximately at 1480 cm^{-1} (Ren et al. 2006; Zaman et al. 2012). The spectrum of DACNC showed a peak referring to the carbonyl group (−C=O−) at 1720 cm^{-1}, confirming the introduction of aldehyde groups into the CNC structure through periodate oxidation. However, this peak is very weak, considering the small amounts of aldehyde incorporated into the matrix. Regarding the hydrogels, the new peak at 1644 cm^{-1} indicates the presence of a C=N stretching vibration. This peak strongly supports the formation of imine bonds through Schiff's base reaction, where the –CHO group of DACNC engages with the $–NH_2$ groups of QCS and CMC. Additionally, the peaks at 1730 and 1480 cm^{-1} are present in all hydrogels, confirming the successful addition of QCS into the matrix.

Rheological characterization and printability

The rheological behavior of the hydrogel inks was assessed to evaluate their suitability for 3D printing applications. While secondary cross-linking is often used to address concerns related to the stability and printability of the hydrogels, these

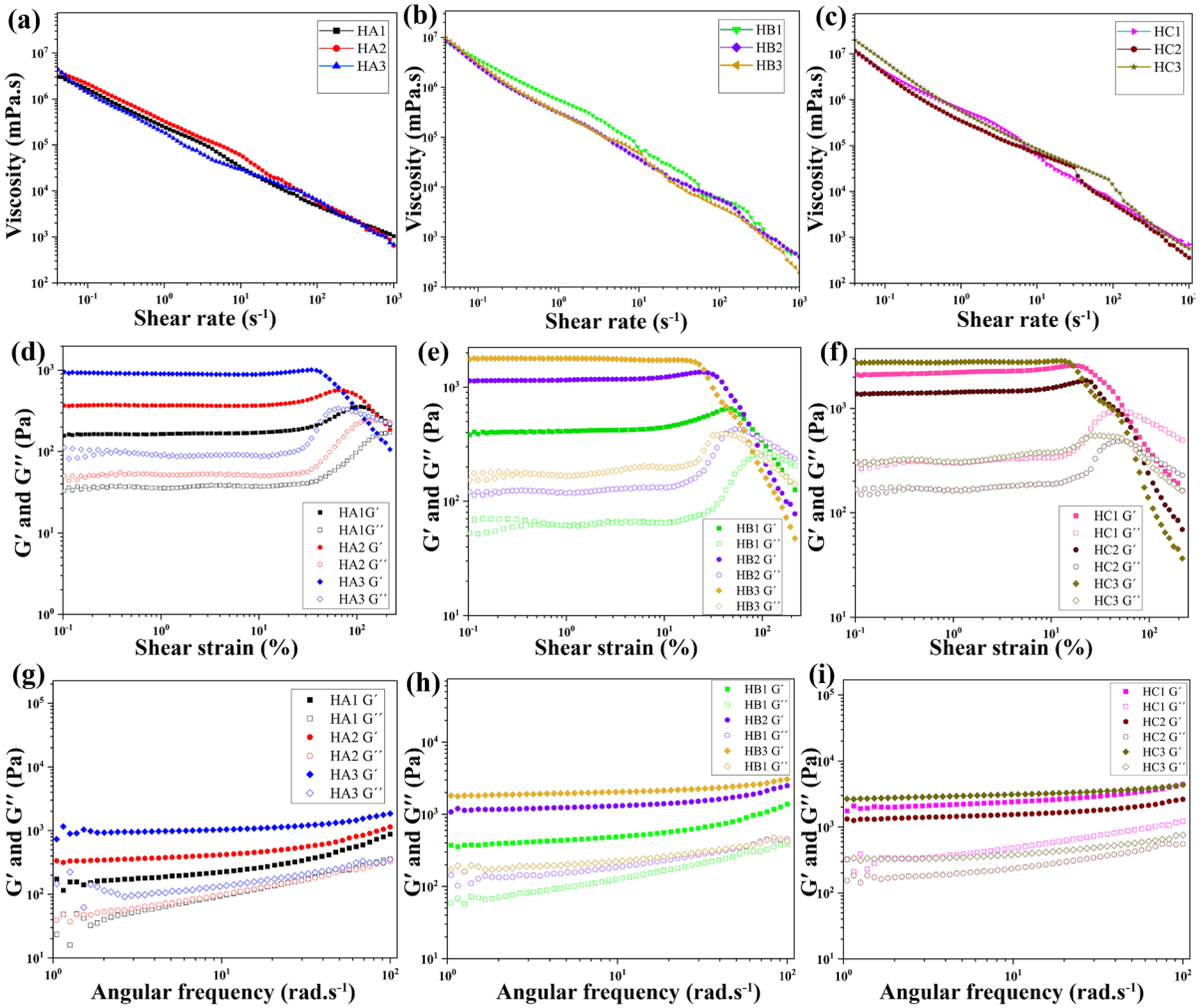

Fig. 3 Rheological characterization of the prepared hydrogel inks before 3D printing. **a–c** The viscosity flow curves of the hydrogel inks as a function of the shear rate with varying amounts of QCS and DACNC. **d–f** Rheological properties (storage and loss moduli (G′ and G″)) of the inks. **g–h** Frequency sweeps of the obtained inks were performed at 0.1% strain

DACNC-CMC-QCS networks eliminate the need for any subsequent cross-linking procedures. Specific rheological characteristics crucial for 3D printing, such as shear thinning, were assessed using a rheometer. Here, high shear rates necessitate low-viscosity behavior for extrusion through fine printing nozzles, while low shear rates require higher viscosity and paste-like behavior to retain the printed 3D shapes (Zhang et al. 2018). As depicted in Fig. 3a–c, the viscosity of the hydrogels decreased significantly with increasing shear rate, confirming their shear-thinning behavior. Notably, hydrogels with higher QCS and DACNC (HC3) concentrations demonstrated elevated viscosity values across the shear rate range. Further, increased DACNC concentrations intensified the shear-thinning effect, indicating enhanced cross-linking between the aldehyde and amine groups. These shear-thinning properties render the hydrogels suitable for use as injectable materials, as demonstrated qualitatively in Fig. S4a by their ability to pass through a plastic catheter and needle without clogging.

The rheological properties of the inks further revealed varying yield strains, as depicted in Fig. 3d–f, and suggested that the material was cross-linked immediately after preparation. As the strain increased, the storage modulus (G′), indicating the elastic modulus, decreased for all inks. In contrast, the loss modulus (G″), representing the viscous modulus, increased. The intersection between G′ and G″ indicated the material's yield point, where the material transitions from a predominantly solid-like behavior to a more viscous and liquid-like state. This further confirms a shear-thinning response. At higher strains, G″ surpassed G′, suggesting disruption of the internal polymer structure. However, the parallel alignment of G′ and G″ at lower shear strains suggests immediate gel network formation upon preparation. These networks broke down at higher strains but exhibited recovery due to self-healing hydrogen bonding. Increased concentrations of QCS led to a more significant difference between G′ and G″, indicating enhanced elastic behavior and overall stiffness of the material. This may improve the mechanical strength and stability of the obtained hydrogel (Elhefian and Yahaya 2010). Similarly, the addition of DACNC increased both G′ and G″, indicating a more cross-linked and reinforced structure. Furthermore, frequency sweeps showed that both G′ and G″ were independent of angular frequency with no crossovers, suggesting stable gel formation over the tested range (Fig. 3g–i). In addition, both G′ and G″ increased with DACNC content, confirming the reinforcing and cross-linking effect of DACNC in the polymer matrix.

Given the shear-thinning and viscoelastic properties, the gels undergo structural rearrangement under shear forces, making them suitable for applications requiring injectability and mechanical support. Several parameters, including pressure, nozzle diameter, stage speed, and temperature, were optimized for successful 3D printing of the hydrogel inks, here evaluated on hydrogels HA1, HA2, and HA3. HA demonstrated gel formation within 90 to 150 s (Table 2), making them suitable for printing without nozzle clogging. HA1 exhibited fully interconnected grid structures, although some collapse was observed in the internal pores. In contrast, HA2 and HA3 demonstrated uniform structures without collapse, remaining individualized throughout, highlighting their suitability for 3D printing applications (Fig. S4). However, HB and HC faced challenges due to their short gelation times of less than 30 s. Also, the higher concentrations of QCS in HB and HC led to clogged nozzles after just one printing layer.

Self-healing properties of the hydrogels

Self-healing capabilities are essential for wound healing materials, especially where frequent replacements are necessary due to ruptures (Du et al. 2019; Yang et al. 2021). Self-healing hydrogels can spontaneously restore their structural integrity and mechanical strength even after experiencing damage. Furthermore, these hydrogels offer promising layer-by-layer 3D printing, as the printed layers can seamlessly adhere to each other after printing. Both macroscopic self-healing tests and rheological recovery experiments were conducted to evaluate the hydrogel's self-healing capabilities. In the macroscopic test, illustrated on HA2 (Fig. 4a), two hydrogel disks were prepared, with one dyed blue for clarity, and then sliced into two separate pieces. Subsequently, these divided halves were reconnected to each other. After allowing them to integrate for 1 h in ambient

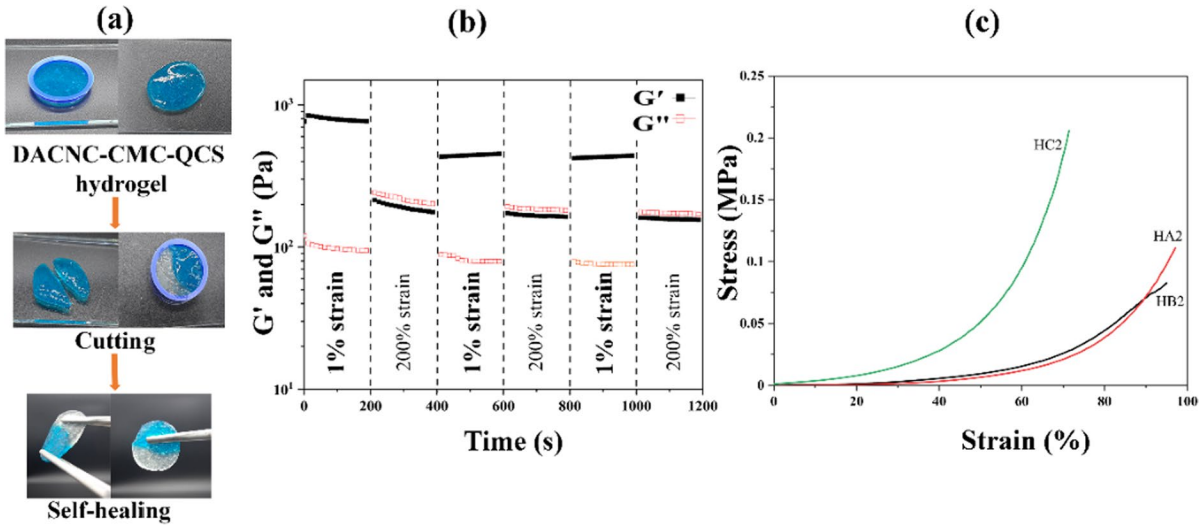

Fig. 4 **a** Photographs depicting the self-healing process of a DACNC-CMC-QCS hydrogel after being cut into two equal segments and fused. **b** Rheological profile of the HA2 hydrogel under an alternating step strain, transitioning between 1 and 200% at intervals of 200 s, illustrating the hydrogel's ability to restore its mechanical integrity following deformation. **c** Compression stress–strain curves of HA2, HB2, and HC2

conditions, the boundaries between the hydrogel pieces became imperceptible, and the original shapes of the pieces were fully restored. Further confirmation of the self-healing process was demonstrated by using tweezers to hold the two sides of the healing incision. The self-healing mechanism of the hydrogel relies on imine and hydrogen bonds, which function as reversible chemical and physical interactions within the hydrogel network, thereby orchestrating the remarkable self-healing properties observed in the material. In a rheological recovery assessment, a continuous cycle of oscillatory strain was employed to analyze the rheological behavior of the HA2 hydrogel ink (Fig. 4b). Notably, when subjected to a higher shear strain of 200%, the loss modulus (G″) surpassed the storage modulus (G′), indicating a transition in behavior where the hydrogel started behaving more like a liquid due to the disruption of its network structure. However, upon subsequent exposure to a 1% strain, the G′ value of the hydrogel rapidly increased, almost fully restoring its initial modulus in a remarkably short time. This suggests that the hydrogel has a certain degree of resilience and can recover its viscoelastic properties after deformation due to reversible structural properties. The mechanical properties of hydrogels HA2, HB2, and HC2 were further examined through a compressive test, as illustrated in Fig. 4c. During the test, the samples demonstrated good stability and remained intact without breaking. In the linear region, when stress was applied, the relaxed hydrogel transitioned to a stressed state, initiating elastic deformation to store energy and counteract the compressive stress. The compression stress at 60% strain for HA2, HB2, and HC2 was 0.011 MPa, 0.015 MPa, and 0.095 MPa, respectively. These results indicate that increasing the QCS ratio (HC2) enhances crosslinking, resulting in a stiffer hydrogel.

SEM analysis

SEM was used to study the microstructure of freeze-dried hydrogel scaffolds and investigate the porosity and pore sizes in a dry state. Figure 5 shows the SEM images of lyophilized hydrogels taken from the surface and cross-section. The hydrogels depicted, HA2, HB2, and HC2, have increased concentrations of QCS, whereas the amounts of DACNC and CMC were kept constant. Each lyophilized hydrogel had rough surfaces and a porous structure, ideal characteristics to facilitate the wound-healing process. The pores in HB2 were smaller and denser than in HA2. Based on these observations, the QCS was successfully crosslinked with DACNC, and the crosslink density increased with the increasing QCS content

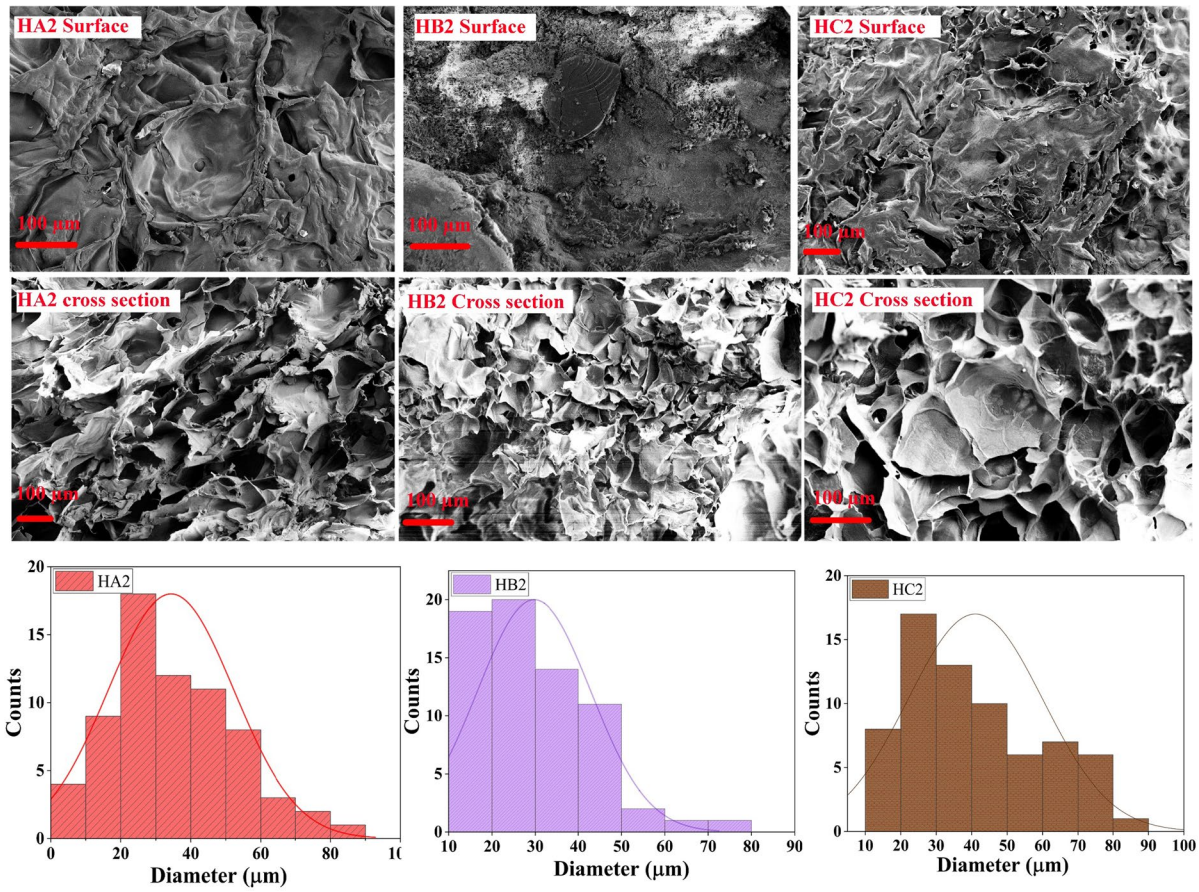

Fig. 5 SEM images of freeze-dried hydrogel scaffolds (HA2, HB2, and HC2) showing the surface and cross-sectional areas and the pore size distributions

in HB2. However, in HC2, the pores grew with additional QCS concentrations, whereas the pore density decreased. The increase in pore size of the HC2 may be due to a lower degree of crosslinking compared to HB2, as more free amine groups were available for crosslinking since the CMC and DACNC concentrations were kept constant.

Swelling capacity and degradation of dried hydrogels

Hydrogel swelling is a critical factor in managing wound exudates and maintaining an optimal moist environment during the healing process. Striking a delicate balance is essential—not allowing the wound to become dehydrated while also preventing the accumulation of excessive exudate, which could disrupt the extracellular matrix. Figure 6a illustrates the swelling ratios of the lyophilized hydrogel samples in aqueous solution. All hydrogels exhibited rapid swelling, with the curves stabilizing after 4 h. HA displayed a greater increase in the swelling capacity compared to HB and HC, indicating that the addition of QCS to the network matrix decreased the swelling tendencies. Similarly, the amount of DACNC in the hydrogel also reduced the swelling. This may be attributed to the high density of a cross-linked network. Crosslinking contributes to increased hydrogel stiffness and reduces swelling propensity. Consequently, the HC3 hydrogel, containing the highest concentrations of QCS and DACNC, exhibited the lowest swelling ratios. Mass changes were monitored for

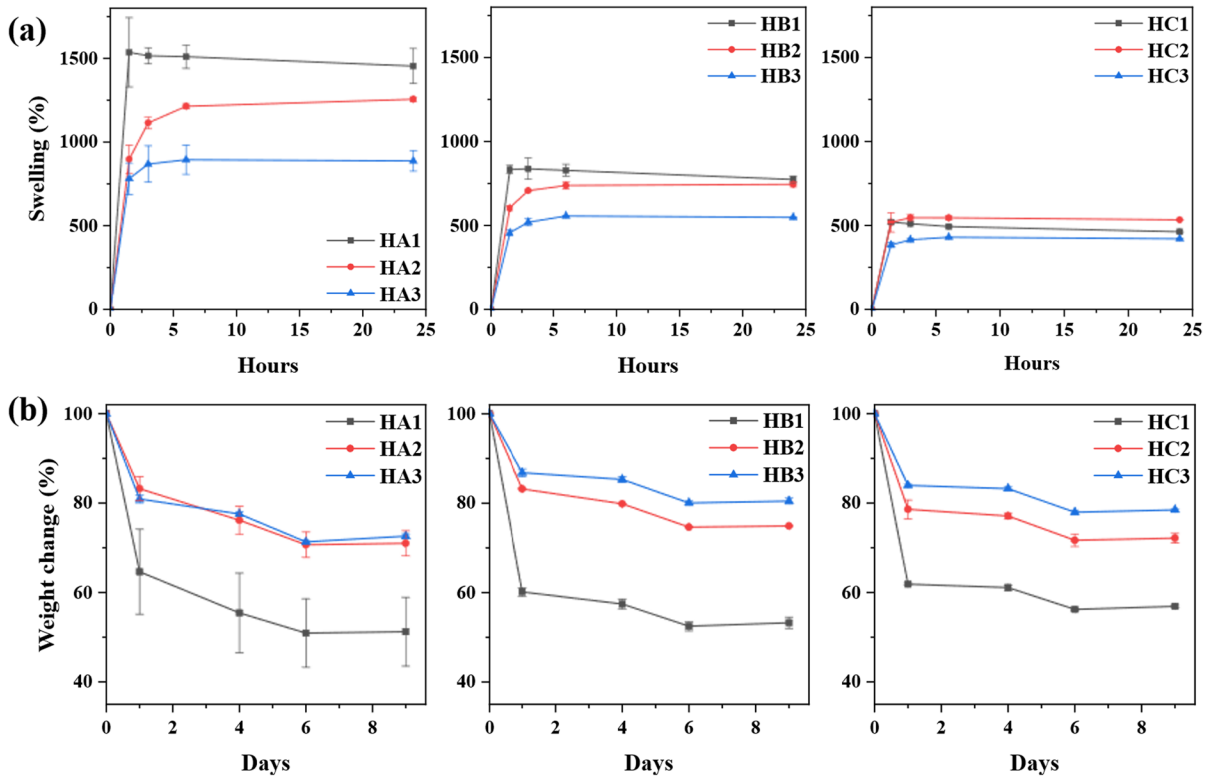

Fig. 6 **a** Swelling ratio, and **b** weight loss of the 3D-printed freeze-dried hydrogels when submerged in a buffer. [$n = 3$, average ± SD]

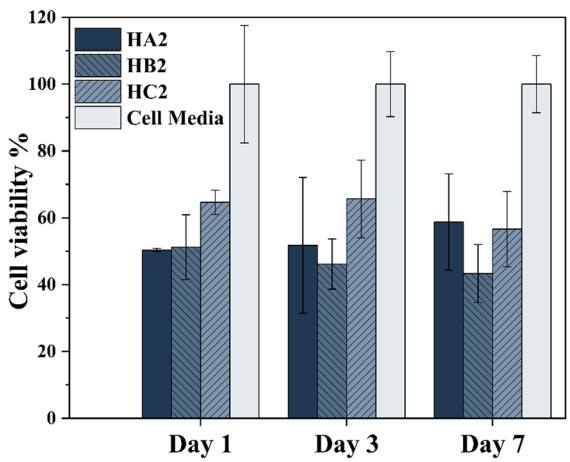

Fig. 7 The relative viability of HDF cells cultured on the hydrogels for 1, 3, and 7 days and assessed with an Alamar Blue assay. [n = 3, average ± SD]

the in vitro assessment of hydrogel biodegradability in aqueous solution (pH 7.4). As illustrated in Fig. 6b, after 9 days of immersion, hydrogels containing the lowest amount of DACNC (HA1, HB1, and HC1) experienced a weight loss of approximately 50–55%. Notably, with increasing amounts of DACNC, the weight loss changes decreased by 15–25%. The network's stability was significantly influenced by the density of cross-links: higher cross-link density correlated with lower levels of degradation. During the initial 24 h, the weight loss is presumably due to the removal of uncross-linked polysaccharide fractions rather than degradation.

In vitro biocompatibility

The hydrogel's biocompatibility and potential cytotoxicity were evaluated in vitro on human dermal fibroblast cells using an Alamar Blue assay. The hydrogels exhibited minor autofluorescence at 560 nm (Fig. S5), which was considered by including control wells containing hydrogels without cells. As quaternary chitosan possesses excellent biocompatibility

(Ahmadi et al. 2015), particular attention was paid to assessing the concentration of QCS in the hydrogels. Therefore, hydrogels HA2, HB2, and HC2 were explicitly chosen for evaluation, as the concentrations of QCS varied while maintaining constant amounts of DACNC and CMC. The fibroblasts cultured on these hydrogels showed cell viability ranging from 43 to 66% after 1, 3, and 7 days of incubation, compared to the control wells (Fig. 7). Notably, HC2 showed overall higher cell viability than HB2 and HA2, which is consistent with our expectations as HC2 contained elevated concentrations of QCS. Furthermore, QCS derivatives have been reported to differ in biocompatibility depending on various factors, such as the degree of quaternization, cationic strength, and molecular weight. It has been observed that with an

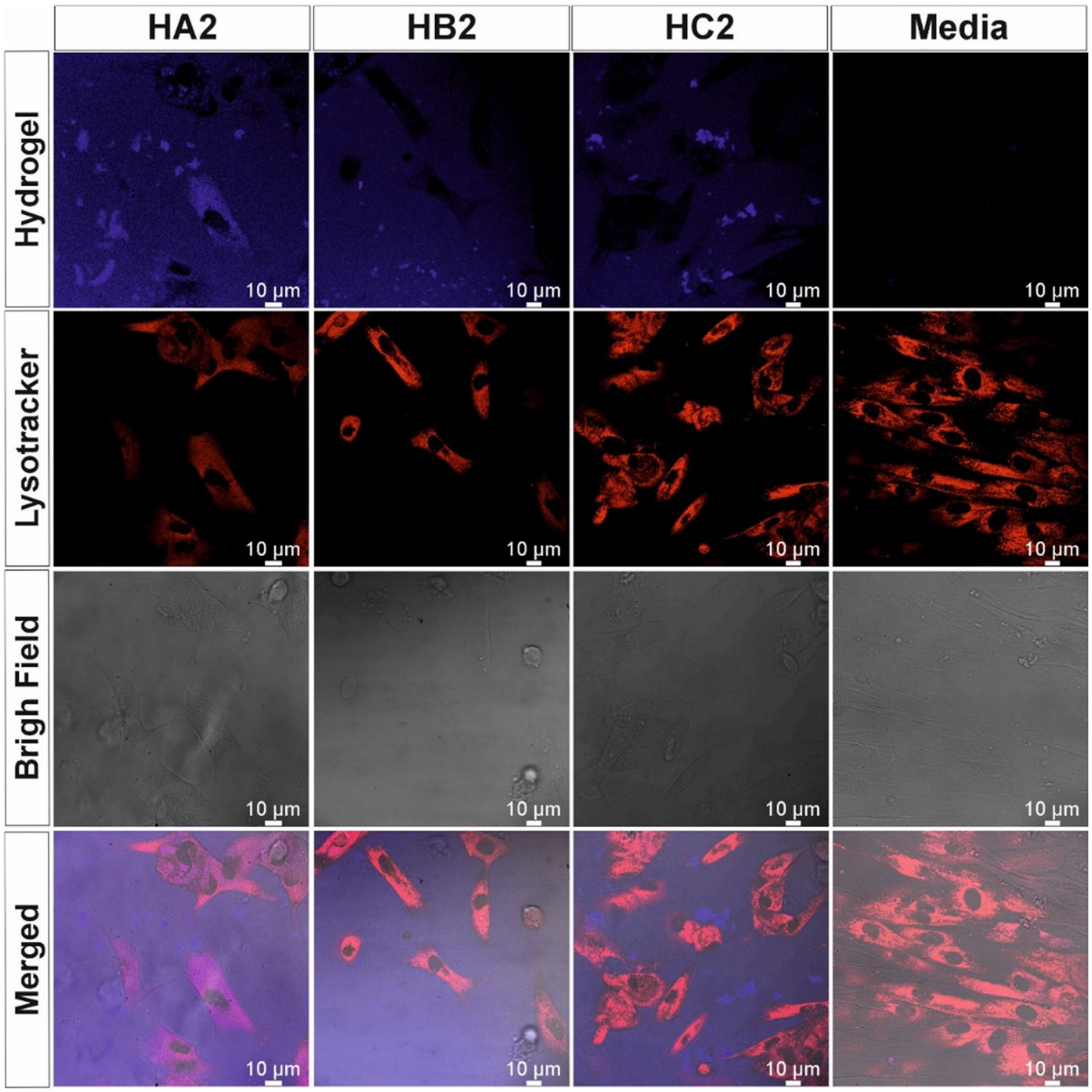

Fig. 8 CLSM images depicting HDF cells incubated on hydrogels HA2, HB2, and HC3 for 24 h. Living cells were stained red using LysoTracker™ Deep Red, while the hydrogels are represented in blue

increasing degree of quaternization, there is a corresponding increase in cytotoxicity (Harugade et al. 2023; Wongwanakul et al. 2017). In this study, the degree of quaternization of QCS in the hydrogels was estimated to be 1.4, falling within the higher range of quaternization. This parameter likely contributes to the observed differences in cell viability between the three hydrogels and the control wells. However, the cell viability of HC2 remained around 60% throughout the evaluation, whereas the hydrogels HA2 and HB2 had lower viability during the earlier stages. This indicates a stable and biocompatible hydrogel, where the chitosan shows good biocompatibility against fibroblasts.

Although the hydrogels exhibited autofluorescence in both blue and green wavelengths, the strongest fluorescence was observed in blue (Fig. S5). The autofluorescence of the hydrogels may be attributed to the intrinsic properties of chitosan and cellulose derivatives, as certain functional groups within these compounds can emit light. Conjugated groups, such as imine bonds, could potentially contribute to the observed fluorescence (Li et al. 2022; Mi 2005). While fluorescent hydrogels can offer applications in biomedical fields for monitoring movements, healing processes, and molecule detection, a comprehensive evaluation of this phenomenon would be necessary to understand the potential of a fluorescent hydrogel fully. Furthermore, to visualize the interaction between the cells and the hydrogels, LysoTracker™ Deep Red was employed to locate the cell lysosomes (Fig. 8). The samples were imaged using two excitation wavelengths of 405 nm for the hydrogels and 630 nm for the cells. It was observed that the cells tended to grow around the hydrogel rather than within it, with no detected cell growth inside the hydrogel pores. Still, the cells exhibited excellent growth on the hydrogels, indicating favorable material biocompatibility for cell culturing or wound healing applications. For a more thorough comprehension of the biocompatibility between the material and living tissue, further comprehensive evaluations and in vivo studies are required. However, this study was primarily focused on a preliminary proof-of-concept assessment, emphasizing comprehensive material characterization, printability, and initial biocompatibility evaluations, and thus did not extend to such explorations.

Conclusion

In this study, we have successfully developed a hydrogel characterized by multiple cross-links, demonstrating rapid self-healing abilities and excellent printability. Comprised of QCS, CMC, and dialdehyde-modified CNC, this hydrogel offers several advantages for biomedical applications. It utilizes water as a solvent, undergoes rapid gelation, and does not require external stimuli such as pH, temperature, or light for cross-linking. The inclusion of stiff DACNC served as both cross-linkers and nano-reinforcement, facilitating rapid gelation due to their numerous active cross-linking sites. The gelation time decreased with increasing concentrations of QCS and DACNC, following Schiff's base reaction principles for imine bond formation. These hydrogels exhibit shear-thinning behavior and impressive self-healing capabilities, restoring structural integrity and mechanical strength after damage. Adding QCS and DACNC influences the swelling and degradation tendencies, with higher cross-link density resulting in reduced swelling and degradation. In vitro cell viability evaluation demonstrated excellent biocompatibility with human fibroblast cells after 7 days, suggesting a potential for wound healing applications. Interestingly, the hydrogels exhibited slight fluorescence at certain wavelengths, a desirable attribute in the biomedical field. In conclusion, these DACNC-CMC-QCS hydrogels offer a promising material for biomedical applications, providing a unique combination of rapid self-healing, printability, and tunable properties to support various wound-healing and tissue engineering efforts.

Acknowledgments The authors would like to thank Svenska Kulturfonden (ID 176261), Competence Center for Materials Bioeconomy, FinnCERES (ID 318891), and ValueBiomat (ID 327248) for providing funding and Ph.D. scholarships for this project. Imaging was performed at the Light Microscopy Unit, Institute of Biotechnology, supported by HiLIFE and Biocenter at the University of Helsinki. This work made use of the BIOECONOMY infrastructure at Aalto University.

Author contributions M.M. and I.L. contributed equally to this work. Conceptualization: M.M., I.L., S.B., and J.S.; methodology: M.M., I.L., S.B., and Z.G.; investigation: M.M., I.L., and Z.G.; writing (original draft): M.M., I.L., and Z.G.; writing (review and editing): M.M., I.L., S.B., Z.G., and N.L.; supervision: T.L., N.L., and J.S.; funding and acquisition: J.S.

Funding Open Access funding provided by Aalto University. FinnCERES,318891,ValueBiomat,327248,Svenska Kulturfonden,176261

Data availability No datasets were generated or analysed during the current study.

Declarations

Conflict of interest The authors declare no competing interests.

References

Ahmadi F, Oveisi Z, Mohammadi Samani S, Amoozgar Z (2015) Chitosan based hydrogels characteristics and pharmaceutical applications. Res Pharmaceut Sci 10(1):1–16

Baniasadi H, Ajdary R, Trifol J, Rojas OJ, Seppälä J (2021) Direct ink writing of aloe vera/cellulose nanofibrils biohydrogels. Carbohyd Polym. https://doi.org/10.1016/j.carbpol.2021.118114

Borandeh S, Laurén I, Teotia A, Niskanen J, Seppälä J (2023) Dual functional quaternary chitosans with thermoresponsive behavior: structure–activity relationships in antibacterial activity and biocompatibility. J Mater Chem B. https://doi.org/10.1039/D3TB02066E

Dang X, Liu P, Yang M, Deng H, Shan Z, Zhen W (2019) Production and characterization of dialdehyde cellulose through green and sustainable approach. Cellulose 26(18):9503–9515. https://doi.org/10.1007/S10570-019-02747-9/FIGURES/8

Du S, Chen X, Chen X, Li S, Yuan G, Zhou T, Li J, Jia Y, Xiong D, Tan H (2019) Covalent chitosan–cellulose hydrogels via schiff-base reaction containing macromolecular microgels for pH-sensitive drug delivery and wound dressing. Macromol Chem Phys. https://doi.org/10.1002/macp.201900399

Elhefian EA, Yahaya A (2010) Rheological study of chitosan and its blends: an overview. Maejo Int J Sci Technol 4(02):210–220

Fan J, Shi Z, Lian M, Li H, Yin J (2013) Mechanically strong graphene oxide/sodium alginate/polyacrylamide nanocomposite hydrogel with improved dye adsorption capacity. J Mater Chem A 1(25):7433–7443. https://doi.org/10.1039/C3TA10639J

Fan L, He Z, Peng X, Xie J, Su F, Wei DX, Zheng Y, Yao D (2021) Injectable, intrinsically antibacterial conductive hydrogels with self-healing and pH stimulus responsiveness for epidermal sensors and wound healing. ACS Appl Mater Interfaces 13(45):53541–53552. https://doi.org/10.1021/ACSAMI.1C14216/ASSET/IMAGES/LARGE/AM1C14216_0009.JPEG

Hamedi H, Moradi S, Hudson SM, Tonelli AE (2018) Chitosan based hydrogels and their applications for drug delivery in wound dressings: a review. Carbohyd Polym 199:445–460. https://doi.org/10.1016/j.carbpol.2018.06.114

Harugade A, Sherje AP, Pethe A (2023) Chitosan: a review on properties, biological activities and recent progress in biomedical applications. React Funct Polym 191:105634. https://doi.org/10.1016/j.reactfunctpolym.2023.105634

Huang Y, Zhang X, Wu A, Xu H (2016) An injectable nano-hydroxyapatite (n-HA)/glycol chitosan (G-CS)/hyaluronic acid (HyA) composite hydrogel for bone tissue engineering. RSC Adv 6(40):33529–33536. https://doi.org/10.1039/C5RA26160K

Huang W, Wang Y, Huang Z, Wang X, Chen L, Zhang Y, Zhang L (2018) On-demand dissolvable self-healing hydrogel based on carboxymethyl chitosan and cellulose nanocrystal for deep partial thickness burn wound healing. ACS Appl Mater Interfaces 10(48):41076–41088. https://doi.org/10.1021/acsami.8b14526

Janarthanan G, Tran HN, Cha E, Lee C, Das D, Noh I (2020) 3D printable and injectable lactoferrin-loaded carboxymethyl cellulose–glycol chitosan hydrogels for tissue engineering applications. Mater Sci Eng C. https://doi.org/10.1016/j.msec.2020.111008

Kim SW, Kim DY, Roh HH, Kim HS, Lee JW, Lee KY (2019) Three-dimensional bioprinting of cell-laden constructs using polysaccharide-based self-healing hydrogels. Biomacromol 20(5):1860–1866. https://doi.org/10.1021/ACS.BIOMAC.8B01589/ASSET/IMAGES/LARGE/BM-2018-01589J_0005.JPEG

Li S, Pei M, Wan T, Yang H, Gu S, Tao Y, Liu X, Zhou Y, Xu W, Xiao P (2020) Self-healing hyaluronic acid hydrogels based on dynamic Schiff base linkages as biomaterials. Carbohyd Polym. https://doi.org/10.1016/j.carbpol.2020.116922

Li D, Liang X, Zhang F, Li J, Zhang Z, Wang S, Li Z, Xing Y, Guo K (2022) Imine bond orientation manipulates AIEgen derived Schiff base isomers through the intramolecular hydrogen bond effect for different fluorescence properties and applications. J Mater Chem C 10(30):11016–11026. https://doi.org/10.1039/d2tc01890j

Lin P, Ma S, Wang X, Zhou F, Lin P, Ma S, Wang X, Zhou F (2015) molecularly engineered dual-crosslinked hydrogel with ultrahigh mechanical strength, toughness, and good self-recovery. Adv Mater 27(12):2054–2059. https://doi.org/10.1002/ADMA.201405022

Lu T, Li Q, Chen W, Yu H (2014) Composite aerogels based on dialdehyde nanocellulose and collagen for potential applications as wound dressing and tissue engineering scaffold. Compos Sci Technol 94:132–138. https://doi.org/10.1016/J.COMPSCITECH.2014.01.020

Mi FL (2005) Synthesis and characterization of a novel chitosan-gelatin bioconjugate with fluorescence emission. Biomacromol 6(2):975–987. https://doi.org/10.1021/bm049335p

Qing X, He G, Liu Z, Yin Y, Cai W, Fan L, Fardim P (2021) Preparation and properties of polyvinyl alcohol/N–succinyl chitosan/lincomycin composite antibacterial hydrogels for wound dressing. Carbohyd Polym. https://doi.org/10.1016/j.carbpol.2021.117875

Quan L, Xin Y, Wu X, Ao Q (2022) Mechanism of self-healing hydrogels and application in tissue engineering. Polymers. https://doi.org/10.3390/polym14112184

Ren JL, Sun RC, Liu CF, Chao ZY, Luo W (2006) Two-step preparation and thermal characterization of cationic 2-hydroxypropyltrimethylammonium chloride hemicellulose polymers from sugarcane bagasse. Polym Degrad Stab 91(11):2579–2587. https://doi.org/10.1016/j.polymdegradstab.2006.05.008

Segal L, Creely JJ, Martin AE, Conrad CM (1959) An empirical method for estimating the degree of crystallinity of native cellulose using the X-Ray diffractometer. Text Res J 29(10):786–794. https://doi.org/10.1177/004051755902901003

Teotia A, Lauren I, Borandeh S, Seppala J (2023) Quaternized chitosan derivatives as viable antiviral agents : 2 structure—activity correlations and mechanisms of action. ACS Appl Mater Interfaces 15:18707–18719. https://doi.org/10.1021/acsami.3c01421

Wang XH, Song F, Qian D, He YD, Nie WC, Wang XL, Wang YZ (2018) Strong and tough fully physically crosslinked double network hydrogels with tunable mechanics and high self-healing performance. Chem Eng J 349:588–594. https://doi.org/10.1016/J.CEJ.2018.05.081

Wang Z, An G, Zhu Y, Liu X, Chen Y, Wu H, Wang Y, Shi X, Mao C (2019) 3D-printable self-healing and mechanically reinforced hydrogels with host–guest non-covalent interactions integrated into covalently linked networks. Mater Horiz 6(4):733–742. https://doi.org/10.1039/C8MH01208C

Wei X, Cai J, Wang C, Yang K, Ding S, Tian F, Lin S (2022) Quaternized chitosan/cellulose composites as enhanced hemostatic and antibacterial sponges for wound healing. Int J Biol Macromol 210:271–281. https://doi.org/10.1016/j.ijbiomac.2022.05.007

Wongwanakul R, Jianmongkol S, Gonil P, Sajomsang W, Maniratanachote R, Aueviriyavit S (2017) Biocompatibility study of quaternized chitosan on the proliferation and differentiation of Caco-2 cells as an in vitro model of the intestinal barrier. J Bioact Compat Polym 32(1):92–107. https://doi.org/10.1177/0883911516658780

Xu J, Liu Y, Hsu S (2019) Hydrogels based on schiff base linkages for biomedical applications. Molecules. https://doi.org/10.3390/MOLECULES24163005

Yang X, Li P, Tang W, Du S, Yu M, Lu H, Tan H, Xing X (2021) A facile injectable carbon dot/oxidative polysaccharide hydrogel with potent self-healing and high antibacterial activity. Carbohyd Polym. https://doi.org/10.1016/j.carbpol.2020.117040

Zaman M, Xiao H, Chibante F, Ni Y (2012) Synthesis and characterization of cationically modified nanocrystalline cellulose. Carbohyd Polym 89(1):163–170. https://doi.org/10.1016/j.carbpol.2012.02.066

Zhang Z, Jin Y, Yin J, Xu C, Xiong R, Christensen K, Ringeisen BR, Chrisey DB, Huang Y (2018) Evaluation of bioink printability for bioprinting applications. Appl Phys Rev 5(4):041304. https://doi.org/10.1063/1.5053979

Zhou Q, Yang K, He J, Yang H, Zhang X (2019) A novel 3D-printable hydrogel with high mechanical strength and shape memory properties. J Mater Chem C 7(47):14913–14922. https://doi.org/10.1039/C9TC04945B